Precipitate characteristics and synergistic strengthening realization of graphene nanoplatelets reinforced bimodal structural magnesium matrix composites

S.L. Xiang, X.S. Hu, X.J. Wang, L.D. Wang, K. Wu

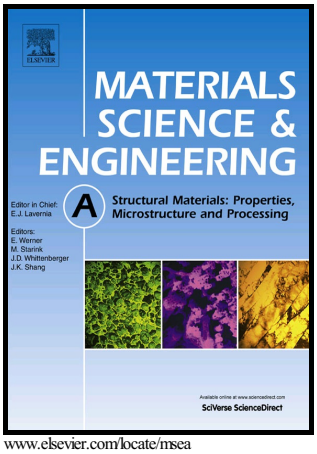

www.elsevier.com/locate/msea

PII: S0921-5093(18)30477-5
DOI: https://doi.org/10.1016/j.msea.2018.03.107
Reference: MSA36300

To appear in: *Materials Science & Engineering A*

Received date: 2 November 2017
Revised date: 16 February 2018
Accepted date: 27 March 2018

Cite this article as: S.L. Xiang, X.S. Hu, X.J. Wang, L.D. Wang and K. Wu, Precipitate characteristics and synergistic strengthening realization of graphene nanoplatelets reinforced bimodal structural magnesium matrix composites, *Materials Science & Engineering A,* https://doi.org/10.1016/j.msea.2018.03.107

Precipitate characteristics and synergistic strengthening realization of graphene nanoplatelets reinforced bimodal structural magnesium matrix composites

S.L. Xiang, X.S. Hu, X.J. Wang*, L.D. Wang, K. Wu

School of Materials Science and Engineering, Harbin Institute of Technology, 92 West Da-Zhi Street, Harbin 150001, P.R. China

**Corresponding author. Tel: +86 45186402291. E-mail address: xjwang@hit.edu.cn (X.J. Wang).*

Abstract

This study investigates the precipitation behavior in the graphene nanoplatelets (GNPs) reinforced bimodal structural Mg-6Zn (wt.%) matrix composite. The GNPs with an increasing content progressively accelerate the age-hardening response in the local regions of the composite. The composite takes only half the time that the Mg-6Zn alloy needs to reach the peak strength when aging at 200 ^{o}C. The observation reveals that the planar and wrinkled GNPs in the composite act as the effective trigger of dislocations and collector of solute atoms to accelerate the precipitation. It is concluded that GNPs have a pronounced effect on the development of matrix microstructure. Moreover, the orientation relationship between the aligned GNPs towards the extrusion direction and the matrix grains with a fiber type texture makes the GNPs and $[0001]_{Mg}$ precipitate rods constitute a hybrid strengthening architecture in the composite. As a result, the synergistic strengthening effect of the GNPs and the precipitates is realized.

Keywords: Metal matrix composites; Graphene; Precipitation; Mechanical properties

1. Introduction

Graphene nanoplatelets (GNPs, multilayer graphene typically consists of 10-100 layers) have attracted much attention as a promising reinforcement because of the superior mechanical, electrical and thermal properties [1, 2]. In particular, the two-dimensional structure and super high aspect ratio enable GNPs more favorable to transfer stress, electrons or phonons than other widely used reinforcements [2-5]. For example, GNPs reinforced magnesium (Mg) matrix composites has emerged as an important class of new materials [6-11]. The introduced GNPs in pure Mg and Mg alloys have improved their mechanical properties significantly, which expedite the development of Mg-based structural materials with energy efficiency in the automotive and aerospace industries [12, 13]. However, most alloys are heat treated before use in practice. The strengthening effect of some Mg alloy-based composites is not fully achieved without the subsequent heat treatment. It is also believed that the matrix of the discontinuously reinforced system is highly sensitive to the reinforcements [14]. Hence, it is important to study the aging behavior in the GNPs reinforced Mg matrix composites in order to expand their potential for structural applications.

There are a few early investigations on the aging behavior of Mg matrix composites reinforced by the micro-sized spherical or whisker-like fillers [15-20]. Most results reported that the aging response was accelerated by the addition of the reinforcements [15, 17-20]. On the other hand, some authors claimed that the composites showed little alteration in the aging hardening [16]. It is obvious that no consensus has been reached regarding the effect of reinforcements on the aging behavior of Mg matrix composites. GNPs, which possess the unique two-dimensional and wrinkled structure, is distinctive from the traditional reinforcements. The effect of GNPs on the precipitation process in the Mg alloys needs to be clarified. To date, the limited research papers of the GNPs reinforced Mg alloy matrix composites only reported the enhanced mechanical properties by the addition of GNPs without the heat treatment

[7-10]. As a consequence, experimental support for the precipitate characteristics in the system of GNPs-Mg alloys is still lacking.

In our previous research, the heterogeneous dispersed GNPs reinforced bimodal structural Mg-6Zn (wt.%) matrix composites, where the GNPs were distributed in the GNPs-rich and GNPs-lean regions [10]. For the Mg-6Zn alloy, one of the most commonly used aging hardened Mg alloys, the precipitation process has been studied in detail by many authors [21-23]. In summary, the supersaturated Mg-6Zn solid solution decomposes into two metastable phases, the monoclinic β_1' (Mg_4Zn_7) and the hexagonal β_2' ($MgZn_2$), at 200 ^oC before forming the β equilibrium phase (MgZn or Mg_2Zn_3). Most of the β_1' phase, which forms as the rod precipitate along $[0001]_{Mg}$ (referred to as $[0001]_{Mg}$ rod), is considered responsible for the strengthening effect in the Mg-6Zn alloy and even the Mg-Zn-based alloys [24]. Owing to the concentration gradient of GNPs in the composite, the effect of GNPs on precipitation hardening of the Mg-6Zn alloy can vary in different local regions. Therefore, the bimodal structure of GNPs reinforced Mg-6Zn composite provides insights into the influence of GNPs on the precipitation behavior of the Mg matrix composites. Very recently, attempts in tailoring the carbon nanofiller (carbon nanotubes + GNPs) revealed the significant hybrid strengthening ability in metal matrix composites [25-27]. However, the design of GNPs-precipitate hybrid reinforced Mg matrix composites is still rare. The interconnected network of planar GNPs and precipitates offers an inspiration to realize the synergistic strengthening architecture in the GNPs reinforced Mg-6Zn matrix composites.

Accordingly, this paper investigates the precipitation behavior of the 0.7 vol.% GNPs reinforced Mg-6Zn bimodal structural composite and the pure Mg-6Zn alloy by the microhardness evaluation, microstructural characterization and tensile test. The results demonstrate that the GNPs with an increasing content gradually promote the precipitation hardening response in local areas. Under the same heat treatment

conditions, the composite takes only half the time that the Mg-6Zn alloy needs to reach the peak strength. The process of the GNPs assisted precipitation is discussed based on the experimental evidence. It is concluded that the synergistic strengthening effect is realized in the composite by the hybrid reinforcement network of GNPs-$[0001]_{Mg}$ precipitates.

2. Materials and Methods

2.1 Materials fabrication

The raw materials used were the pure Mg ingot and the pure Zn ingot from Yueyang Aerospace New Materials Co. Ltd. (P.R. China). The GNPs were purchased from Knano Co. Ltd. (P.R. China) by the thermal reduction of graphite oxide. According to the data sheet, the thickness of GNPs was less than 10 nm and the mean planar diameter ranged from 1-3 μm. The 0.7 vol.% GNPs reinforced Mg-6Zn matrix composite was fabricated by the multi-step dispersion method, which includes pre-dispersing of GNPs, semi-solid stirring, high energy ultrasonic processing and hot extrusion. The detailed parameters were discussed elsewhere and hence omitted in this work for brevity [10]. In order to identify the effects of GNPs on the precipitation hardening behavior, the monolithic Mg-6Zn alloy was also fabricated using the same experimental parameters.

2.2 Aging of the GNPs/Mg-6Zn composite

The composite and the alloy were solution heat treated at 340 ^{o}C for 3 h in the muffle furnace and quenched in water at room temperature to retain the solid solution. Aging heat treatment was then performed at 200 ^{o}C for times ranging from 1 h to 24 h in the oven.

2.3. Analysis of microstructure and mechanical properties

The field-emission scanning electron microscopy (SEM) (JSM-5800 LV, JEOL) was

used to study the microstructure of the composite. The evolution of Vickers hardness of the alloy and the composite were measured under loads of 245.2 mN with a dwelling time of 15 s, using a Shimadzu HMV automatic digital microhardness tester. Macrotexture analysis of the Mg-6Zn alloy and the composite were operated by a PANalytical PW3211 X-ray diffractometer on the extrusion-transverse direction (ED–TD) planes (40 kV, 40 mA, Cu Kα radiation). Grain characteristics and the microtexture were examined by the electron backscatter diffraction (EBSD) analyses under a voltage of 12 kV in Oxford Instruments Aztec 2.0 system. The cross-sectional samples for EBSD were mechanically ground and mirror-polished carefully followed by electrolytic polishing in the electrolyte of 37.5 vol.% phosphoric acid and 62.5 vol.% ethanol at 0.3-0.5 A at room temperature for 30-60 s. The transmission electron microscopy (TEM) (JEM 2100, JEOL and Talos F200x, FEI) was used to evaluate the precipitates. The specimens for TEM test were prepared by grinding-polishing to produce a foil of 50 μm thickness, followed by ion beam thinning. To measure the particle radius and length, the TEM samples were tilted in such a way that the incident beam was aligned parallel to the $[11\bar{2}0]$ or $[\bar{1}010]$ direction. Raman spectroscopy was performed using a Raman Station (B&WTEK, BWS435-532SY) with a 532 nm wavelength laser corresponding to 2.34 eV to validate the structural integrity of GNPs. The tensile test at ambient temperature was carried out on an Instron 5569 testing machine, in accordance with ASTM: E8/E8M-13a standard. The cross-head speed was 0.5 $mm \cdot s^{-1}$ and the strain rate was 0.5 min^{-1}, respectively. For each aging condition, three alloy samples and three composite samples of the standard dog-bone shape were tested.

3. Results

3.1 Bimodal structure

Fig. 1a and b are the SEM images of the extruded Mg-6Zn and the 0.7 vol.% GNPs reinforced bimodal structural Mg-6Zn matrix composite. The microstructure of the

composite is clearly divided into the GNPs-rich and the GNPs-lean regions along the direction of extrusion (ED) in the composites, as the result of the disintegration and alignment effect on the reinforcement during the hot extrusion [28]. Fig. 2a–d show the inverse pole figures (IPFs) of the extruded Mg-6Zn alloy and GNPs/Mg-6Zn composite as well as the corresponding grain size histograms. The alloy has a completely recrystallized microstructure with an average diameter of grains between 15 to 40 μm. In comparison, the grains of the composite are refined and divided into coarse equiaxed grains (CEG) and ultra-fine grains (UFG). The GNPs obstruct the grain growth during the dynamic recrystallization (DRX). Thus, the bimodal grain size of the composite is achieved owing to the inhomogeneous distribution of GNPs. Fig. 2e displays the distribution of CEG with grain sizes larger than 3 μm after whiting out UFG regions, which reveals that the two areas cluster into long lamellae along ED.

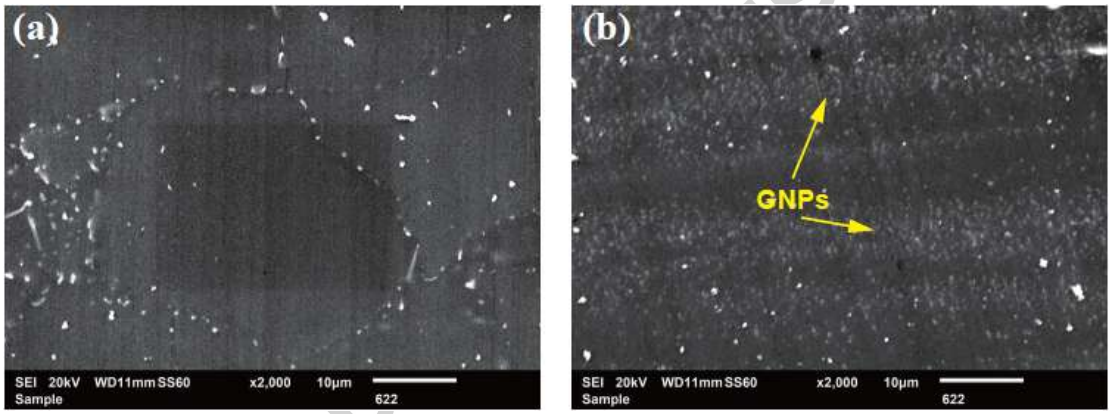

Fig. 1. SEM images of (a) the extruded pure Mg-6Zn alloy and (b) the extruded 0.7 vol.% GNPs reinforced bimodal structural Mg-6Zn matrix composite.

Fig. 3a and b are the {0001} pole figures (PFs) of the extruded Mg-6Zn alloy and the composite measured by means of X-ray diffraction. Both samples show the fiber texture [29]. Because of the addition of GNPs, the composite demonstrates a weaker intensity of the texture than the alloy. The {0001} PFs of the CEG and UFG zones of Fig. 2c are given in Fig. 3c and d, respectively, which also present the fiber type texture. Nonetheless, the basal planes of the grains in the UFG zone distribute in a larger angle away from the normal-transverse direction (ND-TD) plane in the PF, and

the basal poles of the UFG also show a lower intensity than the CEG.

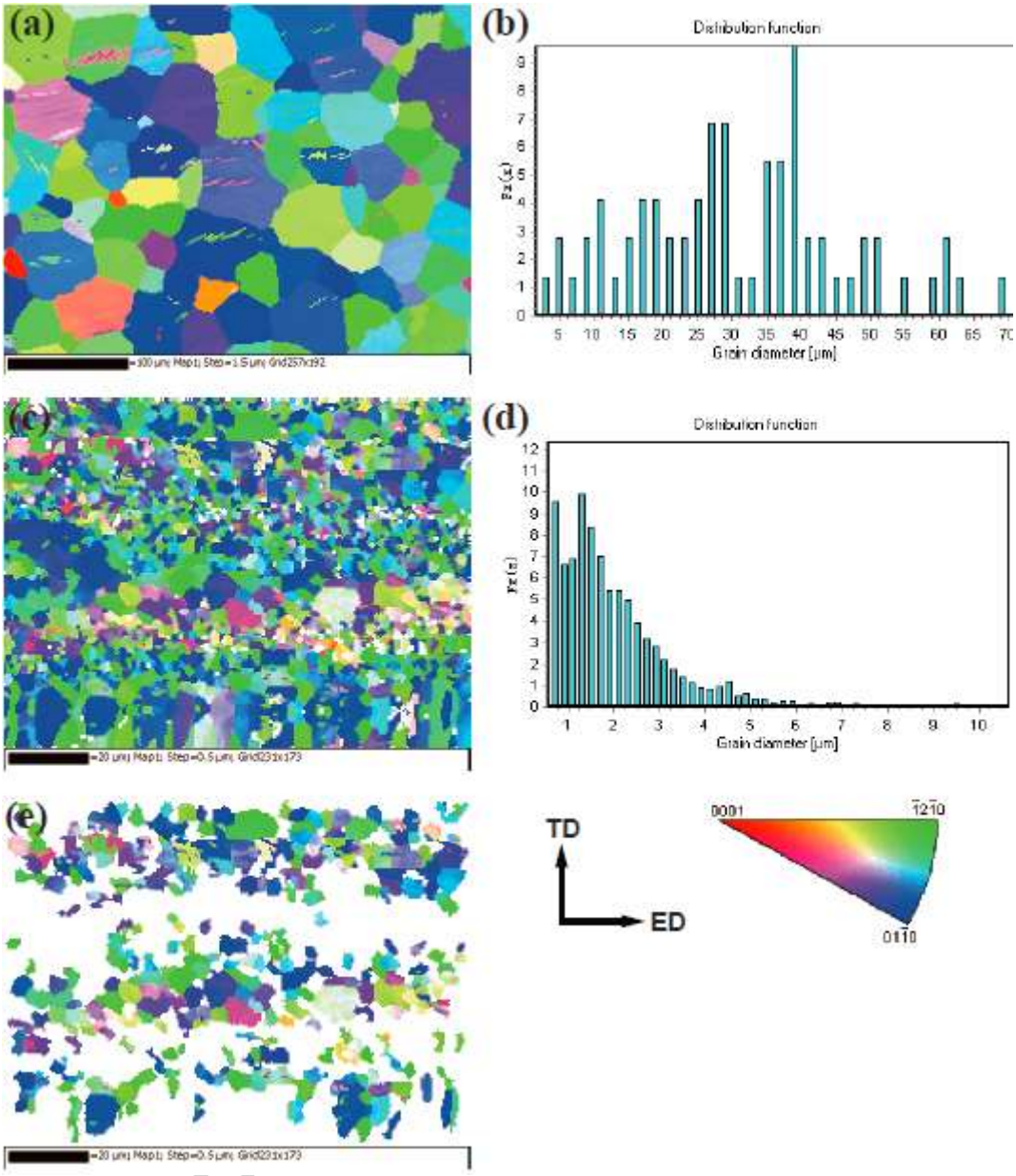

Fig. 2. Grain characteristics by EBSD. (a) and (b) IPF of the extruded Mg-6Zn alloy and the corresponding grain size distribution. (c) and (d) IPF and the grain size distribution of the extruded composite. (e) IPF of the CEG region in (c).

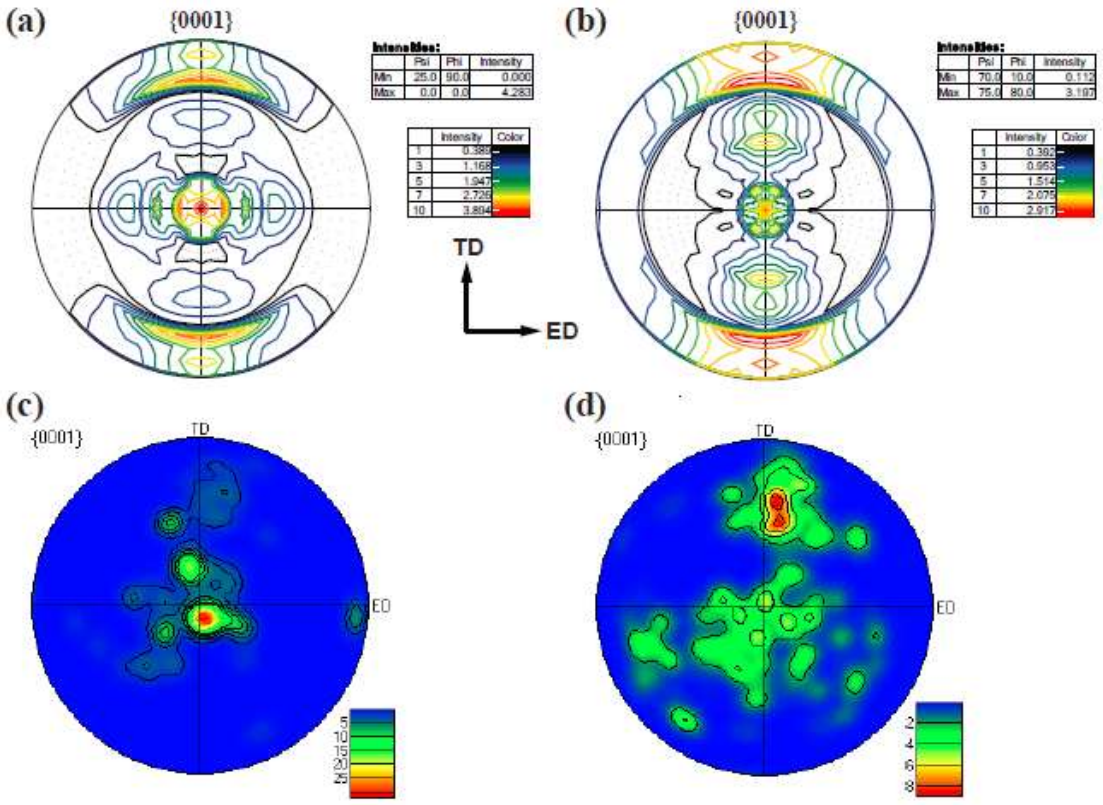

Fig. 3. Texture PFs of the materials. Macrotexture PFs of the extruded (a) Mg-6Zn alloy and (b) the 0.7 vol.% GNPs reinforced composite. Microtexture PFs of the (c) CEG and (d) UFG zones of Fig. 2 (c).

3.2 Aging response

The age hardening responses of the composite and the Mg-6Zn alloy at 200 ^{o}C are shown in Fig. 4. Error bars represent standard deviation (SD) of six experimental points. The hardness of the CEG and UFG in the composite are recorded and plotted separately in Fig 4 because of the bimodal microstructure. The Mg-6Zn alloy exhibits a typical age hardening response and reaches the maximum value when aging for 8 h [21, 30]. On the other hand, both the CEG and UFG regions of the composite show narrow peak hardness changes and reach the maximum hardness values at 4 h. It should be noted that the maximum increase in hardness of the CEG (20 HV) is smaller than that of both the UFG (23 HV) and the Mg-6Zn (22 HV). Considering that the hardness values of CEG at 4 and 6 h are similar, a detailed age hardening response

of the composite from 4 to 6 h is provided in the inset of Fig. 4. The hardness of the CEG shows a plateau at about 4 h 45min. Therefore, if the peak-aged time of the alloy and the composite are arranged in ascending order, the sequence should be: 1) UFG, 2) CEG and 3) Mg-6Zn alloy.

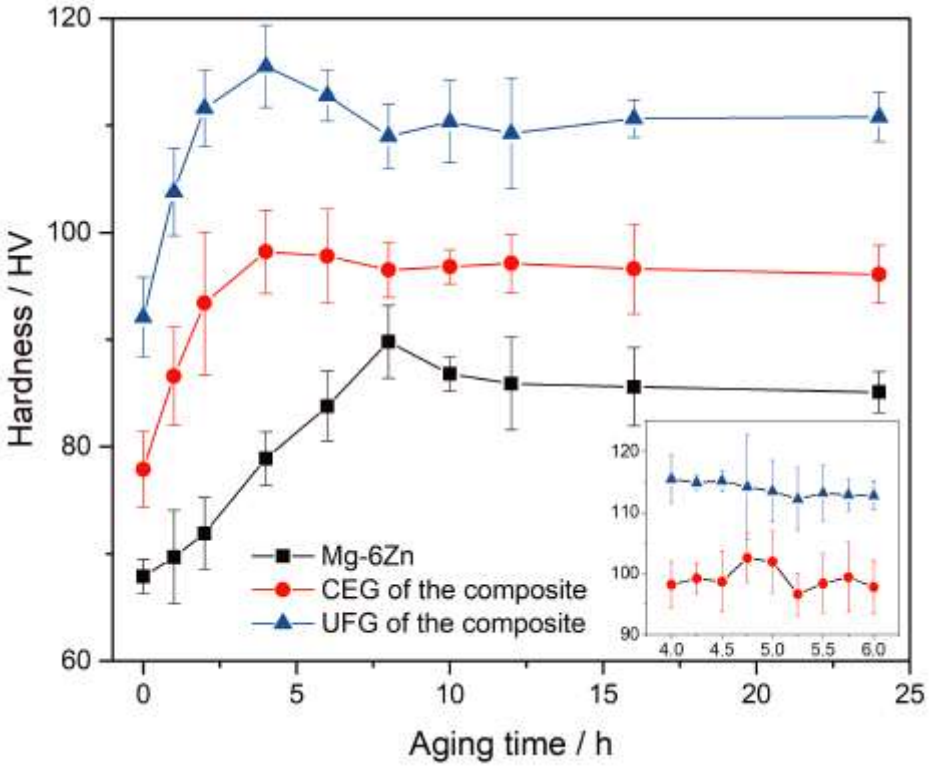

Fig. 4. The measured hardening responses of the Mg-6Zn alloy, CEG and the UFG of the composite, respectively, when aging at 200 ^{o}C. The inset shows the detailed hardening response of the composite aging from 4 to 6 h. Error bars stand for SD of six data sets.

3.3 Precipitates characterization

Fig. 5a shows the bright field TEM image of solution-treated composite without the precipitates. Fig. 5b-f compare the TEM microstructures of the pure Mg-6Zn alloy and the 0.7 vol.% GNPs reinforced Mg-6Zn composite aged for 4 h. It is obvious that the rod-shaped particles are the most common type of precipitate. In the case of the Mg-6Zn alloy (as shown in Fig 5b), the tiny rod-shaped precipitates emerge in the

matrix with a low content. Nevertheless, the micrographs of the UFG grains aged for 4 h (Fig. 5c-e) reveal a much higher density of precipitates. According to the mass-thickness contrast in the TEM image, the embedded GNPs that locate at the grain boundary and in the interior of the grains of Fig. 5c-e are identified by the wrinkled surfaces or edges, as marked by the yellow arrows. Fig. 5d is a typical GNPs induced grain, and Fig. 5e shows the same grain of Fig. 5d when we tilt the foil slightly away from the exact diffraction condition. The broken orange lines are the guidelines to indicate the grain boundaries in Fig. 5d and e, respectively. The discernible GNPs in both Fig. 5d and e are numbered consistently. In Fig. 5c, the precipitate-free zone (PFZ) is formed near the grain boundary. The PFZ is induced by the depletion of excess vacancies at the grain boundary or interface of reinforcement/matrix, because vacancies have a high diffusivity [21, 31]. However, a bundle of precipitate rods extend from the GNPs which lay on the grain boundary. Moreover, there also exist some blocky and coarse Mg-Zn phase around GNPs (Fig. 5c and e), which are generally considered to be formed during the prolonged aging time in the alloy [32]. The typical TEM image of the CEG region aged for 4 h (Fig. 5f) reveals a microstructure that resembles the UFG region.

In order to evaluate the effect of precipitation on the structural integrity of GNPs, the Raman spectrum of the raw GNPs and the composites are given in Fig. 6. The D peak around 1340 cm^{-1} and the G peak around 1585 cm^{-1} correspond to the introduced defects and the vibration in sp^2 bond stretching in graphene, respectively. Hence, the relative intensity ratio of D to G peak (I_D/I_G) indicates the defect density in GNPs [33]. In Fig. 6, the values of I_D/I_G of the GNPs, the as-extruded, solution-treated and aged composite are calculated to be 0.48, 1.00, 1.04 and 1.02, respectively. The increase of I_D/I_G ratio from the raw GNPs to the composites indicates that the fabrication process, such as the high energy ultrasonic vibration and the hot extrusion, has introduced defects and disorders in the graphene. However, the I_D/I_G of the composites at different stages of heat treatment are almost equal, which reveals that the formation of precipitates has little negative influence on the structural integrity of GNPs.

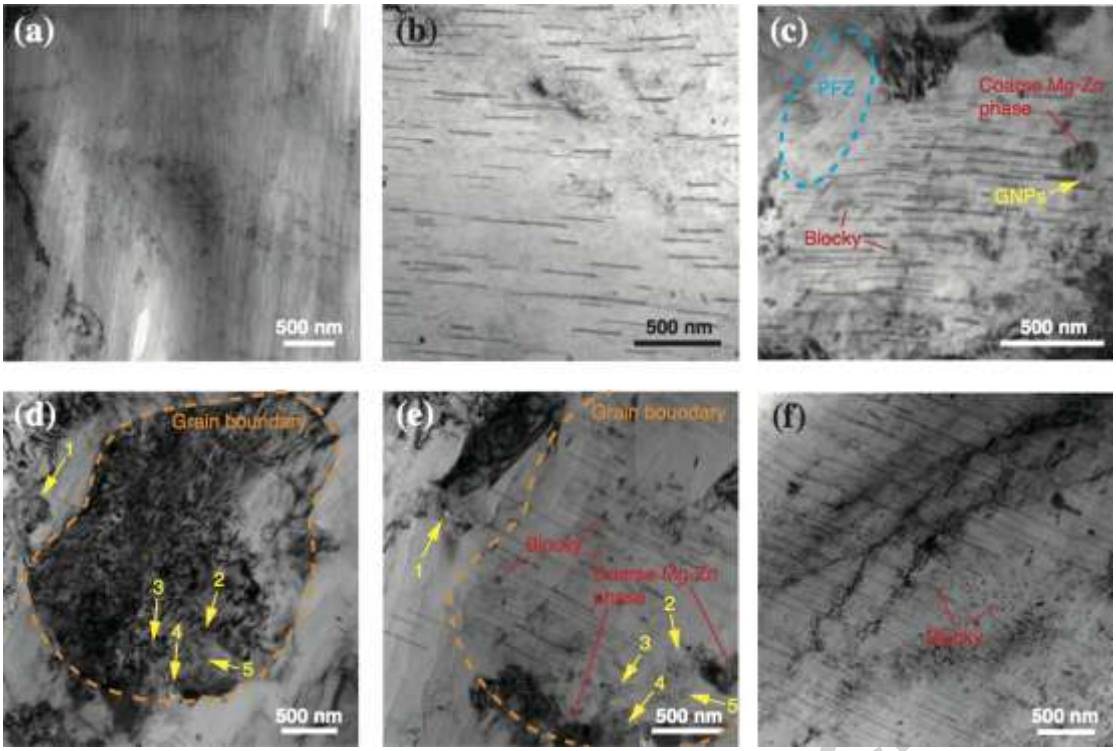

Fig. 5. TEM images of (a) the solution-treated composite. Precipitate morphologies of (b) the Mg-6Zn alloy, (c)-(e) UFG and (f) CEG in the composite aged at 200 ^{o}C for 4 h. The discernible GNPs in both (d) and (e) are numbered consistently.

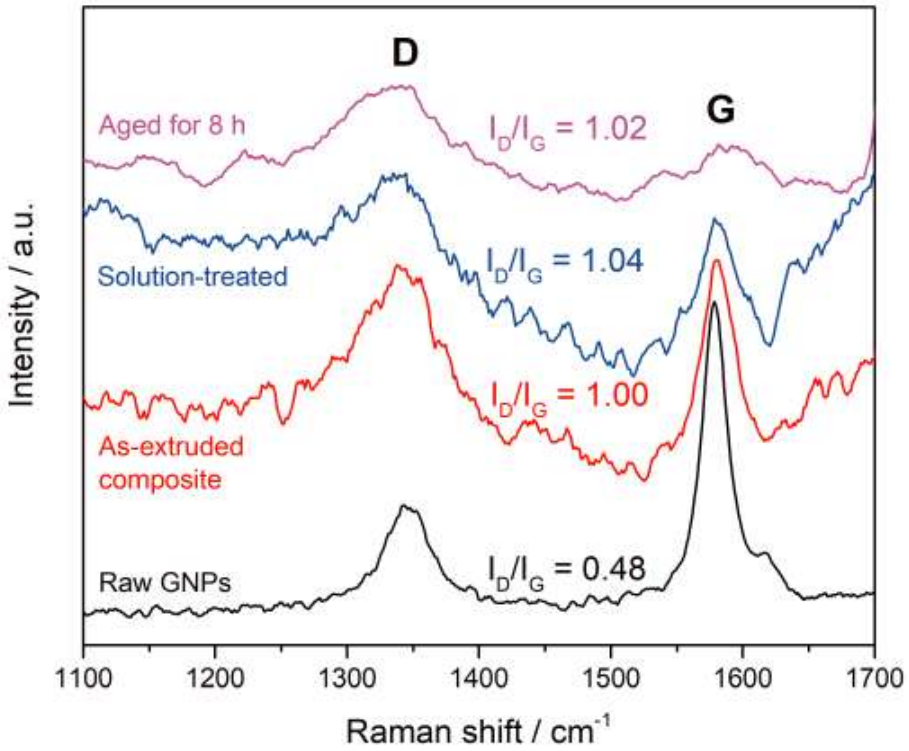

Fig. 6. Raman spectra of the raw GNPs and the composite at the as-extruded, solution-treated and aged conditions.

3.4 Mechanical properties

The engineering tensile stress-strain curves of the alloy and composite aging at 200 ^{o}C for different aging times are shown in Fig. 7a and b, respectively. Table 1 summarizes the yield strength (*YS*), ultimate tensile strength (*UTS*) and fracture elongation (ε_f) of the Mg-6Zn alloy and the composite. The yield strength of every sample is determined using the 0.2 % strain offset method from the stress-strain curve [34]. Regardless of the GNPs, the strength of both the alloy and the composite increases significantly in the initial stage of aging and then decreases slowly. The Mg-6Zn alloy reaches the maximum tensile strength when aged for 8 h and the composite reaches the peak value at 4 h. However, it should be noted that the peak-aged time of CEG (about 4 h 45 min) in the composite is not consistent with the peak-aged time of UFG

(about 4 h) from the hardness analysis. The tensile properties of the composite aged for 4 h and 4 h 45 min reveal little significant distinction, as presented in Fig. 7b and Table 1. Thus the peak-aged time of the whole composite can be regarded as 4 h for simplification. The maximum increase in yield strength of the Mg-6Zn alloy and the composite are 85 (8 h) and 80 (4 h) MPa, respectively. The smaller value of the composite should be attributed to the heterogeneous internal precipitation rate and the premature consumption of Zn around the GNPs in the composite (Fig. 5c and e). In terms of ductility, the composite shows the decreased fracture elongation compared to the Mg-6Zn alloy at all the aging conditions. Despite the sacrifice in the ductility, the composite still presents the typical ductile fracture and acceptable elongation more than 10 % at various aging times.

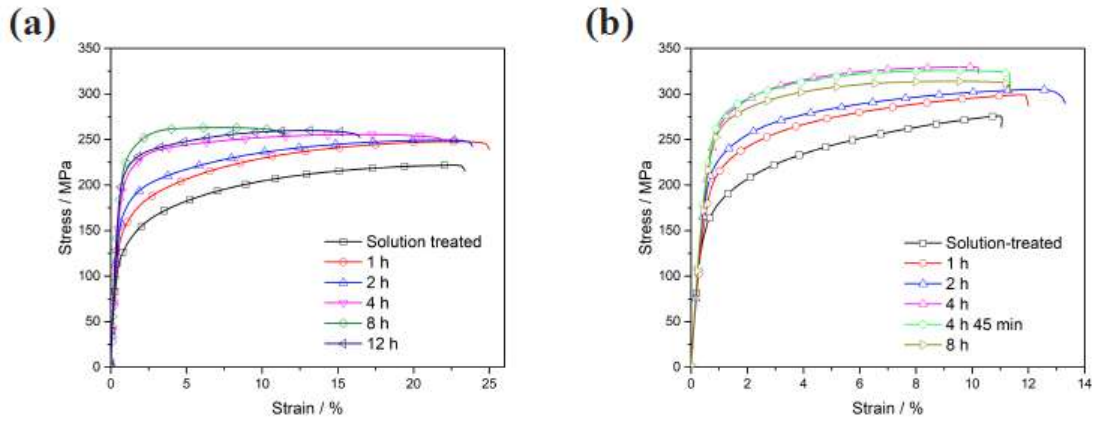

Fig. 7. Tensile curves of (a) the Mg-6Zn alloy and (b) the composite aging at 200 ^{o}C for different aging times.

Table 1. Mechanical properties of the heat-treated Mg-6Zn alloy and 0.7 vol.% GNPs reinforced Mg-6Zn composite.

Materials	Aging time / h	*YS* / MPa	*UTS* / MPa	ε_f / %
Mg-6Zn alloy	Solution-treated	107 ± 5	221 ± 1	23.0 ± 2.9
	1	123 ± 1	248 ± 2	24.5 ± 1.1
	2	141 ± 4	249 ± 3	23.7 ± 2.2
	4	167 ± 5	256 ± 6	21.4 ± 1.0

	8	192 ± 4	263 ± 5	11.0 ± 2.9
	12	183 ± 6	259 ± 6	16.1 ± 3.3
GNPs/Mg-6Zn	Solution-treated	161 ± 3	276 ± 5	11.0 ± 2.8
composite	1	183 ± 6	299 ± 7	11.9 ± 3.9
	2	208 ± 3	305 ± 3	11.4 ± 3.4
	4	241 ± 5	330 ± 6	10.2 ± 4.3
	4.75	242 ± 3	326 ± 4	11.7 ± 3.3
	8	230 ± 6	314 ± 5	11.3 ± 1.5

4. Discussion

4.1 Precipitation behavior

In the composite, the depletion of vacancies and the generation of dislocations at the interface of reinforcement/matrix are two competitive processes that affect the precipitation [35]. The interface of GNPs/matrix is the sink for the excess vacancies in the matrix, however, the excess dislocations can be generated due to the mismatch in coefficient of thermal expansion ($\Delta\alpha$) between the matrix and GNPs. The coefficient of thermal expansion of Mg matrix and GNPs are $\alpha_M = 28.4 \times 10^{-6}$ $(°C)^{-1}$ [36] and $\alpha_{GNPs} = -8 \times 10^{-6}$ $(°C)^{-1}$ [37], respectively. $\Delta\alpha$ equals to $\alpha_M - \alpha_{GNPs}$. Therefore, the nucleation on dislocations should be able to offset the effect of decreased vacancies in the accelerated aging response. Fig. 8a presents a TEM bright-field image contains a piece of GNPs in the composite after solution treatment. The dense tangles of dislocations arrange at the GNPs/matrix interface. When the dislocations are generated around the GNPs, the GNPs are also effective barriers to the propagation and annihilation of dislocations across the interface due to their high intrinsic mechanical strength and the large surface area [38]. Because of the promoted heterogeneous nucleation sites, the GNPs assist in the nucleation of the embryo beyond the critical size [31]. Moreover, GNPs also act as the collector of Zn solute atoms. In order to identify the distribution of elements after the solution treatment, the high angle annular dark field (HAADF) TEM imaging and the element mapping of

Mg, Zn and C of the enlarged Fig. 8a is carefully performed. In Fig. 8b-f, the blue color corresponds to Zn overlaps on parts of the red color corresponds to C, which indicates that Zn segregates on the surface of the GNPs after the solution treatment. The segregation of the Zn solute should be attributed to the interfacial adsorption of GNPs and the high diffusivity paths provided by the dislocations around. As a result, the growth of the precipitates around GNPs can occur at rates far greater than allowed by volume diffusion during aging. Because the GNPs induced dislocations and the solute segregation accelerate the precipitation synergistically, the coarse Mg-Zn phase coincides with the GNPs when aged for only 4 h (Fig. 5c and e). The previous researchers have already revealed that micro-sized reinforcements (such as particles and whiskers) and carbon nanotubes enhanced the nucleation rate of precipitates by the increased density of dislocations [18, 20, 39]. Compared to these reinforcements, the GNPs with abundant wrinkles and edges are superior additives to create not only excess dislocations but also solute segregation at the interfaces. Hence, precipitates are more likely to nucleate on these sites. Fig. 8g schematically displays the possible nucleation process of the $[0001]_{Mg}$ precipitates in the vicinity of GNPs in a Mg crystal unit.

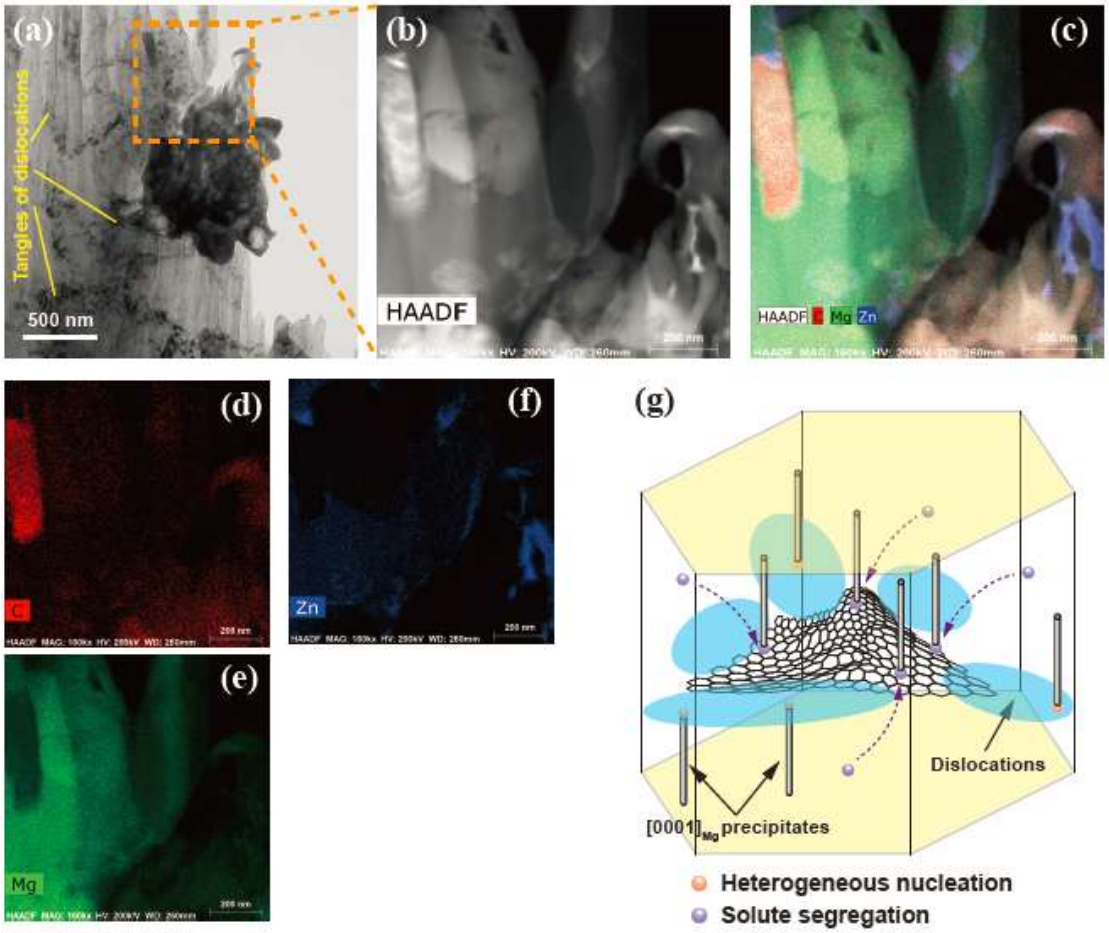

Fig. 8. (a) TEM micrograph of the embedded GNPs in the composite after solution heat treatment. (b) The enlarged HAADF TEM image of (a). (c)-(f) The corresponding elemental mapping of Mg, Zn and C of (b), respectively. (g) The schematic representation of the nucleation process of the $[0001]_{Mg}$ precipitates near the GNPs in a Mg crystal unit.

4.2 Mechanical properties

Fig. 9 shows two TEM micrographs of the deformed composite with the beam directed along the $[0001]_{Mg}$ and $[11\bar{2}0]_{Mg}$, respectively. The $[0001]_{Mg}$ micrograph (Fig. 9a) indicates that the rod precipitates, which are edge-on, effectively block the dislocation slip on the basal planes. The $[11\bar{2}0]_{Mg}$ micrograph (Fig. 9b), where the

$[0001]_{Mg}$ rods are in-plane, indicates that the dislocations move independently between the two rods and do not shear the precipitate rods. In this situation, the effect of Orowan strengthening by the rod precipitates can be achieved. Since the shear-resistant $\beta_1^{'}$ $[0001]_{Mg}$ rods are the main strengthening precipitates, the Orowan strengthening contribution to the yield strength ($\Delta\sigma_{Orowan}$) can be estimated according to the appropriate version of the Orowan equation for $[0001]_{Mg}$ rod precipitate [40]

$$\Delta\sigma_{Orowan} = \frac{MGb}{2\pi d\sqrt{1-v}\cdot\left(\frac{0.953}{\sqrt{V_p}}-1\right)}\ln\frac{d}{b} \quad (1)$$

where M is the Taylor factor (2.1 for the extruded polycrystalline Mg [41]), G is the matrix shear modulus = 17.2 GPa [42], b is the magnitude of the Burgers vector, $|b|$ = 0.32 nm [42], v is the Poisson's ratio (0.35) [42], d is the particle diameter, V_p is the volume fraction of precipitates. In the present work, the volume fraction V_p can be calculated by the following equation when the truncation and overlap corrections are considered [30]:

$$V_p = -\ln(1-A)\cdot\left(\frac{dl}{dl+(d/2+l)T}\right) \quad (2)$$

where A is the projected area faction of the $[0001]_{Mg}$ rods, l is the mean rod length, T is the foil thickness and determined by the convergent-beam electron diffraction (CBED) patterns [43]. The d and l are measured and averaged from at least 100 rods in the TEM images of the CEG and UFG region, respectively. In this way, the determined d and V_p for the CEG and UFG aged for 4 h are 12.6 nm, 1.0 %, 13.3 nm and 1.7 %, respectively. Accordingly, the results of the calculated $\Delta\sigma_{Orowan}$ of CEG and UFG are 77 and 100 MPa, respectively. These two values represent the theoretical lower and upper bound of $\Delta\sigma_{Orowan}$ of the overall composite aged for 4 h. The increased value of yield strength (80 MPa) aged for 4 h stays within the range of the predictions, which confirms that the Orowan mechanism is the main strengthening effect on the increase in yield strength of the heat treated composite. In our previous study of 0.7 vol.% GNPs reinforced bimodal structural Mg-6Zn matrix composite [10],

the composite was mainly strengthened by the grain refinement and the load transfer of the GNPs. The Orowan mechanism contributed by GNPs only took a very little effect (less than 3 MPa) on strengthening among all the factors because of the coarse diameter of GNPs (1-2 μm). On the other hand, the precipitates in the heat treated composite promote the Orowan strengthening effect on basal planes significantly.

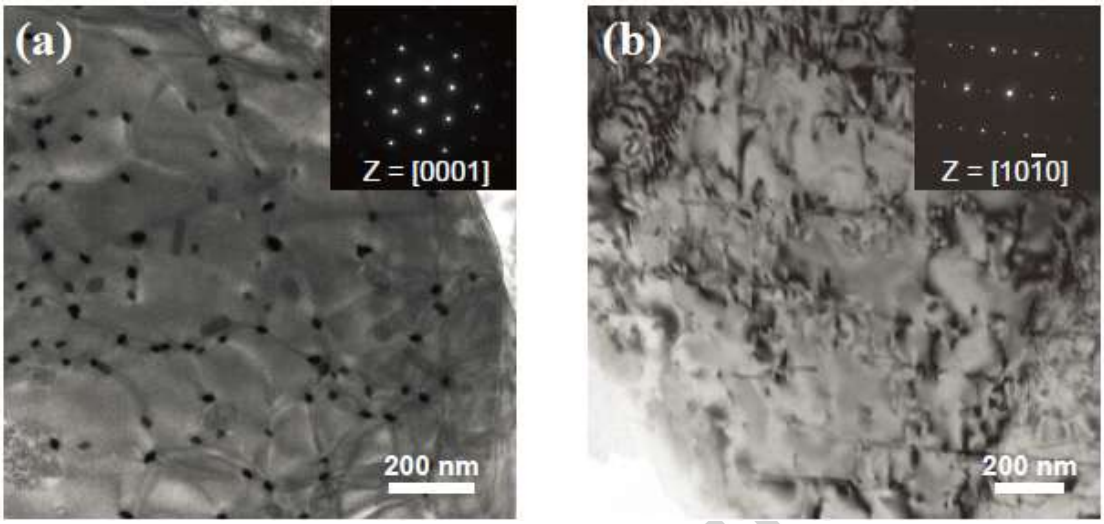

Fig. 9. TEM micrographs of the interaction between the precipitates and dislocations on the (a) basal plane and (b) prismatic plane of the composite. The insets are the corresponding selected area diffraction patterns with the [0001] and [10$\bar{1}$0] zone axis, respectively.

It is common that GNPs lead to the weakened texture during DRX [11]. However, the distribution of crystallographic orientations of the extruded composite still presents the type of fiber texture in the composite (Fig. 3b-d). Fig. 10a describes the hexagonal close-packed (hcp) crystal orientation units in the fiber texture of extrusion. The hcp unites in the composite form the ring of basal planes towards ED, which makes a large proportion of $[0001]_{Mg}$ rods perpendicular to ED (Fig. 10a and b). Moreover, the GNPs are aligned along ED in the as-extruded composite (Fig. 1b). Hence, the GNPs and $[0001]_{Mg}$ rods build a hybrid strengthening network in the three-dimensional space. When an external load is applied to the composite along ED, the GNPs parallel

to ED contribute to the load transfer effect and the $[0001]_{Mg}$ rods perpendicular to ED lead to the Orowan strengthening effect, as illustrated in Fig. 10b.

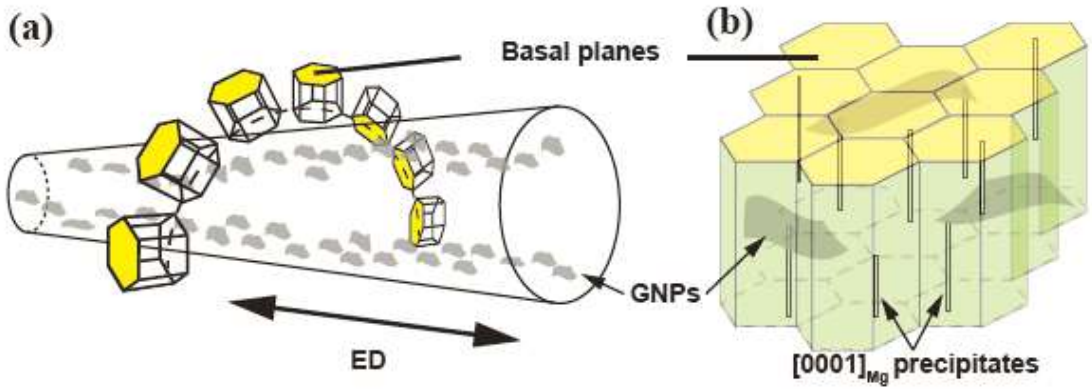

Fig. 10. The schematic representations of (a) the distribution of hcp units in the fiber texture of extrusion and (b) the architecture of the hybrid GNPs-$[0001]_{Mg}$ precipitates in a part of the composite with a fiber texture.

The yield strength comparison of the materials is summarized in Fig. 11. The difference values of yield strength between the composite and the alloy at solution-treated, peak-aged and over-aged states are calculated, respectively. All these three values are around 50 MPa, which are labeled as $\Delta\sigma_1$, $\Delta\sigma_2$ and $\Delta\sigma_3$, respectively, in Fig. 11. These similar difference values obviously derive from the load transfer of GNPs and GNPs induced grain refinement [44], regardless of the aging stages. The previous research has shown that the prior plastic deformation which stimulates a high density of dislocation can also enhance the nucleation rate of precipitates [45]. However, the hardness of the deformed alloys deteriorates significantly at the over-aged stage because of the exhausted dislocations when heated. The finding proves that the deformation-induced dislocations do not itself contribute to hardening during the aging procedure. Indeed, it only affects the precipitation processes during the early stage of aging. In the present study, the composite still holds the notable strength enhancement even during the over-aged stage. Despite the grains of the composite may grow during heating, the load transfer effect of GNPs should be

maintained because of the presence of GNPs with well structural integrity in the aging process. The result shows that the addition of reinforcement is a more reliable approach than plastic deformation to retain the enhanced strength of the composites when the accidental overheating occurs in the industrial application.

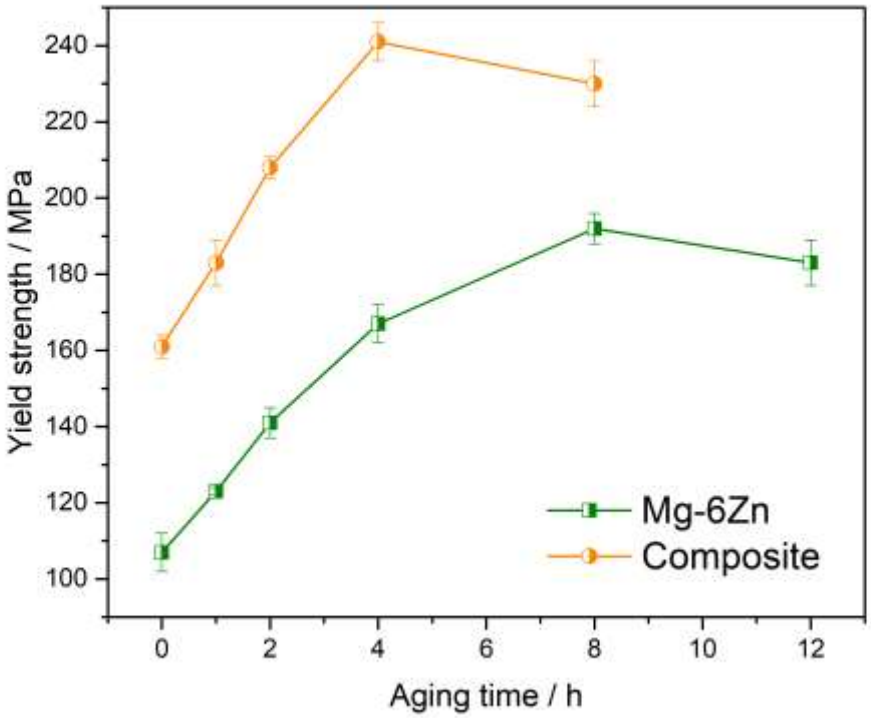

Fig. 11. The comparison of yield strength between the pure Mg-6Zn alloy and the composite at different aging stages. Error bars stand for SD of three data sets.

5. Conclusions

In summary, this paper investigates the effect of GNPs on the precipitate characteristics in the bimodal structural Mg-6Zn matrix composites. The main findings are summarized as follows:

1. The heterogeneous distribution of GNPs in the composite leads to different aging

responses in various local regions. The precipitation rate of $[0001]_{Mg}$ rods in the matrix is gradually accelerated along with the increasing local content of GNPs.

2. GNPs are the effective additives in tuning the development of matrix microstructure. Owing to the planar structure and wrinkled surface, the GNPs promote the generation of dislocations and the segregation of solute atoms.
3. Because of the fiber texture of the extruded composite and the alignment of the GNPs along ED, the hybrid GNPs-$[0001]_{Mg}$ rods assemble an interconnected network of reinforcements in the composite. The load transfer effect of the GNPs and the Orowan strengthening mechanism of the $[0001]_{Mg}$ rod precipitates are combined when the external load is applied to the composite along ED.

Acknowledgement

Support from National Natural Science Foundation of China (Nos. 51671066 and 51471059), National Key Research and Development Plan (Nos. 2017YFB0703102 and 2016YFB0301102) and Key laboratory of Lightweight and high strength structural materials of Jiangxi Province (No. 20171BCD40003) is acknowledged. We also thank Dr. D. Li of National University of Singapore for the assistance in polishing the manuscript.

References

[1] K.S. Novoselov, V.I. Fal'ko, L. Colombo, P.R. Gellert, M.G. Schwab, K. Kim, A roadmap for graphene, Nature 490(7419) (2012) 192-200.

[2] A. Nieto, A. Bisht, D. Lahiri, C. Zhang, A. Agarwal, Graphene reinforced metal and ceramic matrix composites: a review, Int. Mater. Rev. 62(5) (2017) 241-302.

[3] S.C. Tjong, Recent progress in the development and properties of novel metal matrix nanocomposites reinforced with carbon nanotubes and graphene nanosheets, Mater. Sci. Eng. R 74(10) (2013) 281-350.

[4] H. Yang, H. Cui, W. Tang, Z. Li, N. Han, F. Xing, A critical review on research progress of graphene/cement based composites, Compos. Part A Appl. Sci. Manuf. 102 (2017) 273-296.

[5] M. Rashad, F. Pan, M. Asif, X. Chen, Corrosion behavior of magnesium-graphene composites in sodium chloride solutions, J. Magnes. Alloys 5(3) (2017) 271-276.

[6] L.-Y. Chen, H. Konishi, A. Fehrenbacher, C. Ma, J.-Q. Xu, H. Choi, H.-F. Xu, F.E. Pfefferkorn,

X.-C. Li, Novel nanoprocessing route for bulk graphene nanoplatelets reinforced metal matrix nanocomposites, Scr. Mater. 67(1) (2012) 29-32.

[7] M. Rashad, F. Pan, A. Tang, Y. Lu, M. Asif, S. Hussain, J. She, J. Gou, J. Mao, Effect of graphene nanoplatelets (GNPs) addition on strength and ductility of magnesium-titanium alloys, J. Magnes. Alloys 1(3) (2013) 242-248.

[8] M. Rashad, F. Pan, H. Hu, M. Asif, S. Hussain, J. She, Enhanced tensile properties of magnesium composites reinforced with graphene nanoplatelets, Mater. Sci. Eng. A 630 (2015) 36-44.

[9] M. Rashad, F. Pan, M. Asif, Exploring mechanical behavior of Mg–6Zn alloy reinforced with graphene nanoplatelets, Mater. Sci. Eng. A 649 (2016) 263-269.

[10] S.L. Xiang, X.J. Wang, M. Gupta, K. Wu, X.S. Hu, M.Y. Zheng, Graphene nanoplatelets induced heterogeneous bimodal structural magnesium matrix composites with enhanced mechanical properties, Sci. Rep. 6 (2016) 38824.

[11] S.L. Xiang, M. Gupta, X.J. Wang, L.D. Wang, X.S. Hu, K. Wu, Enhanced overall strength and ductility of magnesium matrix composites by low content of graphene nanoplatelets, Compos. Part A Appl. Sci. Manuf. 100 (2017) 183-193.

[12] B. Feng, Y. Xin, F. Guo, H. Yu, Y. Wu, Q. Liu, Compressive mechanical behavior of Al/Mg composite rods with different types of Al sleeve, Acta Mater. 120 (2016) 379-390.

[13] X.J. Wang, D.K. Xu, R.Z. Wu, X.B. Chen, Q.M. Peng, L. Jin, Y.C. Xin, Z.Q. Zhang, Y. Liu, X.H. Chen, G. Chen, K.K. Deng, H.Y. Wang, What is going on in magnesium alloys?, J. Mater. Sci. Technol. In Press, DOI: 10.1016/j.jmst.2017.07.019 (2017).

[14] Q. Chen, G. Chen, F. Han, X.S. Xia, Y. Wu, Microstructures, Mechanical Properties, and Wear Resistances of Thixoextruded SiCp/WE43 Magnesium Matrix Composites, Metall. Mater. Trans. A 48A(7) (2017) 3497-3513.

[15] C. Badini, F. Marino, M. Montorsi, X.B. Guo, Precipitation phenomena in B_4C-reinforced magnesium-based composite, Mater. Sci. Eng. A 157(1) (1992) 53-61.

[16] J. Kiehn, K.U. Kainer, P. Vostry, I. Stulikova, Resistivity changes due to precipitation effects in fibre reinforced Mg Al-Zn-Mn alloy, Phys. Status Solidi A 161(1) (1997) 85-95.

[17] M.Y. Gu, Z.G. Wu, Y.P. Jin, M. Kocak, Effects of reinforcements on the aging response of a ZK60-based hybrid composite, Mater. Sci. Eng. A 272(2) (1999) 257-263.

[18] M.Y. Zheng, K. Wu, S. Kamado, Y. Kojima, Aging behavior of squeeze cast SiCw/AZ91 magnesium matrix composite, Mater. Sci. Eng. A 348(1-2) (2003) 67-75.

[19] X.Q. Zhang, L. Liao, N.H. Ma, H.W. Wang, Effect of aging hardening on in situ synthesis magnesium matrix composites, Mater. Chem. Phys. 96(1) (2006) 9-15.

[20] X.J. Wang, X.S. Hu, W.Q. Liu, J.F. Du, K. Wu, Y.D. Huang, M.Y. Zheng, Ageing behavior of as-cast SiCp/AZ91 Mg matrix composites, Mater. Sci. Eng. A 682 (2017) 491-500.

[21] J.B. Clark, Transmission electron microscopy study of age hardness in a Mg-5 wt.% percent Zn alloy, Acta Metall. 13(12) (1965) 1281-1289.

[22] J.M. Rosalie, H. Somekawa, A. Singh, T. Mukai, The effect of size and distribution of rod-shaped β_1 precipitates on the strength and ductility of a Mg-Zn alloy, Mater. Sci. Eng. A 539 (2012) 230-237.

[23] K. Yan, J. Bai, H. Liu, Z.-Y. Jin, The precipitation behavior of $MgZn_2$ and Mg_4Zn_7 phase in Mg-6Zn (wt.%) alloy during equal-channel angular pressing, J. Magnes. Alloys 5(3) (2017) 336-339.

[24] S. Tekumalla, R. Shabadi, C. Yang, S. Seetharaman, M. Gupta, Strengthening due to the in-situ evolution of ß $_1$ ′ Mg-Zn rich phase in a ZnO nanoparticles introduced Mg-Y alloy, Scr. Mater. 133 (2017) 29-32.

[25] M. Rashad, F. Pan, A. Tang, M. Asif, M. Aamir, Synergetic effect of graphene nanoplatelets (GNPs) and multi-walled carbon nanotube (MW-CNTs) on mechanical properties of pure magnesium, J. Alloys Compd. 603 (2014) 111-118.

[26] Z. Li, G. Fan, Q. Guo, Z. Li, Y. Su, D. Zhang, Synergistic strengthening effect of graphene-carbon nanotube hybrid structure in aluminum matrix composites, Carbon 95 (2015) 419-427.

[27] X. Zhang, C. Shi, E. Liu, F. He, L. Ma, Q. Li, J. Li, N. Zhao, C. He, In-situ space-confined synthesis of well-dispersed three-dimensional graphene/carbon nanotube hybrid reinforced copper nanocomposites with balanced strength and ductility, Compos. Part A Appl. Sci. Manuf. 103 (2017) 178–187.

[28] H.L. Shi, X.J. Wang, C.L. Zhang, C.D. Li, C. Ding, K. Wu, X.S. Hu, A novel melt processing for Mg matrix composites reinforced by multiwalled carbon nanotubes, J. Mater. Sci. Technol. 32(12) (2016) 1303-1308.

[29] Q. Liu, X. Zhou, H. Zhou, X. Fan, K. Liu, The effect of extrusion conditions on the properties and textures of AZ31B alloy, J. Magnes. Alloys 5(2) (2017) 202-209.

[30] J. Jain, P. Cizek, W.J. Poole, M.R. Barnett, Precipitate characteristics and their effect on the prismatic-slip-dominated deformation behaviour of an Mg-6 Zn alloy, Acta Mater. 61(11) (2013) 4091-4102.

[31] D.A. Porter, K.E. Easterling, Phase transformations in metals and alloys, Second ed., Nelson Thornes Ltd, Cheltenham, UK, 2001.

[32] X. Gao, J.F. Nie, Characterization of strengthening precipitate phases in a Mg–Zn alloy, Scr. Mater. 56(8) (2007) 645-648.

[33] A.C. Ferrari, J.C. Meyer, V. Scardaci, C. Casiraghi, M. Lazzeri, F. Mauri, S. Piscanec, D. Jiang, K.S. Novoselov, S. Roth, A.K. Geim, Raman Spectrum of Graphene and Graphene Layers, Phys. Rev. Lett. 97(18) (2006).

[34] J. William D. Callister, Materials science and engineering: an Introduction, John Wiley & Sons, Inc., New York, USA, 2007.

[35] T.W. Clyne, P.J. Withers, An introduction to metal matrix composites, Cambridge University Press, Cambridge, UK, 1993.

[36] M. Gupta, N.M.L. Sharon, Magnesium, magnesium alloys, and magnesium composites, John Wiley & Sons, Hoboken, USA, 2011.

[37] D. Yoon, Y.W. Son, H. Cheong, Negative thermal expansion coefficient of graphene measured by Raman spectroscopy, Nano Lett. 11(8) (2011) 3227-31.

[38] Y. Kim, J. Lee, M.S. Yeom, J.W. Shin, H. Kim, Y. Cui, J.W. Kysar, J. Hone, Y. Jung, S. Jeon, S.M. Han, Strengthening effect of single-atomic-layer graphene in metal–graphene nanolayered composites, Nat. Commun. 4 (2013).

[39] D.H. Nam, Y.K. Kim, S.I. Cha, S.H. Hong, Effect of CNTs on precipitation hardening behavior of CNT/Al-Cu composites, Carbon 50(13) (2012) 4809-4814.

[40] J.F. Nie, Effects of precipitate shape and orientation on dispersion strengthening in magnesium alloys, Scr. Mater. 48(8) (2003) 1009-1015.

[41] C.H. Caceres, P. Lukac, Strain hardening behaviour and the Taylor factor of pure magnesium, Philos. Mag. 88(7) (2008) 977-989.

[42] C.R. Hutchinson, J.F. Nie, S. Gorsse, Modeling the precipitation processes and strengthening mechanisms in a Mg-Al-(Zn) AZ91 alloy, Metall. Mater. Trans. A 36A(8) (2005) 2093-2105.

[43] D.B. Williams, C.B. Carter, Transmission electron microscopy: a textbook for materials science,

Springer, New York, USA, 2009.

[44] H. Yu, C. Li, Y. Xin, A. Chapuis, X. Huang, Q. Liu, The mechanism for the high dependence of the Hall-Petch slope for twinning/slip on texture in Mg alloys, Acta Mater. 128 (2017) 313-326.

[45] M.V.C. Riglos, M.T. de la Cruz, A. Tolley, Accelerated age hardening by plastic deformation in Al-Cu with minor additions of Si and Ge, Scr. Mater. 64(2) (2011) 169-172.